

Senior Honors Thesis (2024)

Understanding Energy Reconstruction in CUORE using Topological Analysis

May 11, 2024

Anisha Krishna Yeddanapudi

University of California, Berkeley



ABSTRACT

CUORE (Cryogenic Underground Observatory for Rare Events), located in the Laboratori Nazionali del Gran Sasso in Italy, is an experiment designed to search for neutrinoless double beta decay ($0\nu\beta\beta$) in ^{130}Te . Neutrinoless double beta decay is a theoretically predicted radioactive decay process that, if observed, would determine the Majorana nature of the neutrino. Experimentally confirming $0\nu\beta\beta$ would signify that neutrinos are their own antiparticle, allowing for a better understanding of the matter-antimatter asymmetry present in the universe. Accurate reconstruction of $0\nu\beta\beta$ event energy is key to isolating $0\nu\beta\beta$ from background events. I performed an analysis of the energy escape events occurring near (~ 1 cm) the surface of the TeO_2 crystals, operated by CUORE. This work aims to understand and correct biases in the bolometric energy reconstruction and improve the systematic uncertainty on the CUORE energy resolution. Currently, there is little microphysical understanding of the energy biases present within the detectors. The analysis aims to classify energy reconstruction errors in terms of event topology, location, and possible variation of the pulse shape. Overall, we find evidence of position-dependent energy reconstruction in TeO_2 bolometers.

ACKNOWLEDGEMENTS

This project is fully funded by the University of California, Berkeley via BPURS (Berkeley Physics Undergraduate Research Scholars). The CUORE Collaboration thanks the directors and staff of the Laboratori Nazionali del Gran Sasso and the technical staff of our laboratories. This work is supported by the US DOE Office of Nuclear Physics, the US NSF, and internal investments at all institutions. This research used resources of the National Energy Research Scientific Computing Center (NERSC). This work makes use of both the DIANA data analysis and APOLLO data acquisition software packages, which were developed by the CUORICINO, CUORE, LUCIFER and CUPID-0 Collaborations.

I would also like to thank Dr. Erin V. Hansen and Prof Yury Kolomensky for their ongoing support throughout this endeavor.

CONTENTS

1	Theoretical Framework	1
1.1	Neutrino Physics	1
1.1.1	A Brief History of the Neutrino	1
1.1.2	Neutrinos & The Standard Model	2
1.1.3	Majorana Neutrinos	3
1.2	Double Beta Decay	3
1.2.1	Neutrinos & Double Beta Decay	3
1.2.2	Neutrinoless Double Beta Decay ($0\nu\beta\beta$)	4
1.3	Experimental Search for $0\nu\beta\beta$	4
2	Background Information	7
2.1	CUORE	7
2.1.1	The CUORE Detector Setup	7
2.1.2	Ge NTDs	10
2.2	CUORE Data	11
2.2.1	Data Collection	11
2.2.2	Calibration	11
2.2.3	Energy Escape Events	12

2.2.4	Coincidence & Multiplicity	13
3	CUORE Data Preliminaries & Characterization	15
3.1	Preliminaries	15
3.1.1	Data Organization & Sorting	16
3.1.2	Two-Dimensional Histograms	17
3.1.3	A Dabble into PCA	18
3.1.4	Box Plots	19
3.2	Gaussian Fits	21
3.2.1	Single Escape Events	22
4	NTD Topology Analysis	27
4.1	Single Escape Events	28
4.1.1	Multiplicity 2	28
4.1.2	Multiplicity 3	31
4.2	Lineshape Analysis	35
5	Conclusion	37
5.1	Future Work	37

CHAPTER 1

THEORETICAL FRAMEWORK

1.1 Neutrino Physics

A neutrino is an elementary particle similar to an electron, but with a neutral charge. Additionally, neutrinos don't exist within atoms, instead, they are created via several processes throughout the Universe [11].

1.1.1 A Brief History of the Neutrino

After the discovery of radioactivity in 1897, many properties of our universe, on a particle and material level, were revealed. However, beta radioactivity remained puzzling. Unlike alpha and gamma decay, where the α or γ particle emitted by a nucleus consisted of only a single energy, the β spectrum was continuous. At the time, this seemed to be a clear contradiction of the fundamental principle of conservation of energy. To help resolve this, Pauli suggested the existence of another particle that was emitted along with the electron to "take away" that excess energy. And so the neutrino was born.

Though Pauli first hypothesized the neutrino's existence, it wasn't until Fermi (who

coined the term 'Neutrino') that it truly became an accepted reality. In 1932, he made the neutrino the basis of his theory of beta decay, showing the simultaneous creation of both the electron and the neutrino. In the decades that followed, beta decay was rigorously studied, and it was discovered that everything was in perfect agreement with Fermi's theory. This all culminated in the experimentally proven existence of the neutrino by Cowan and Reines in 1954. [11]

1.1.2 Neutrinos & The Standard Model

The Standard Model consists of six quarks and leptons (total of 12 particles) which are the building blocks of matter. Charged leptons interact via the weak, electromagnetic, or gravitational forces. Since they never interact through the strong force, leptons are never found inside the nucleus. On the other hand, quarks interact through the strong or color force and have a fractional electric charge. These forces allow quarks to bind together to form neutrons, protons, hadrons, and nuclei. [11]

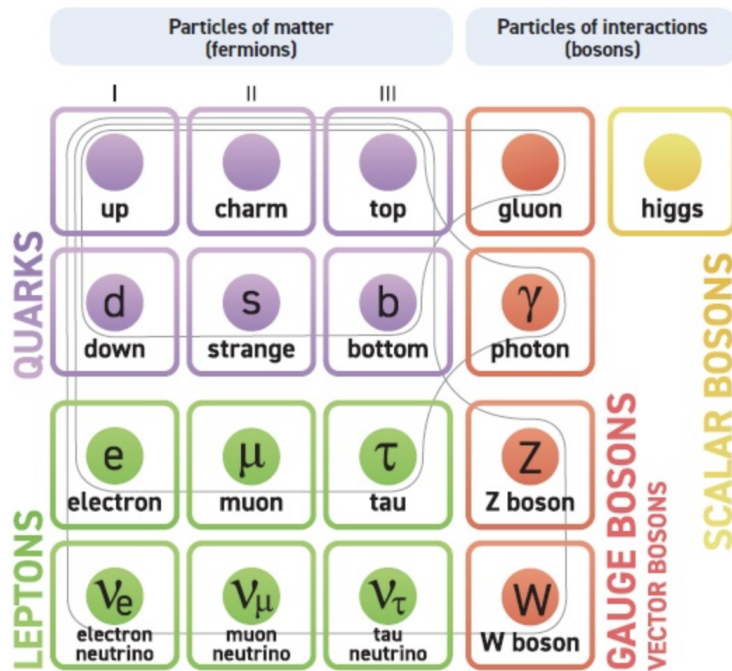


Figure 1.1: Summary schematic of the Standard Model of particle physics.[12]

Neutrinos are also part of the Standard Model. They are characterized as massless, electrically neutral leptons which come in three flavors: the electron, muon, and tau.

Interestingly, the neutrino is one of the few leptons that solely interact with matter through the weak force, making them incredibly difficult to detect [11].

1.1.3 Majorana Neutrinos

When Dirac combined quantum mechanics with relativity, a consequence was that there should be an antiparticle for every particle. For example, the antiparticle of an electron is a positron, the only thing that separates these two is their charge which is equal and opposite. However, the neutrino is neutral, which implies that there is a unique possibility that the neutrino is its own antiparticle. This would mean that the neutrino is a Majorana particle, contrary to an electron whose antiparticle is different. Hence, the electron is characterized as a Dirac particle [11].

1.2 Double Beta Decay

1.2.1 Neutrinos & Double Beta Decay

Nuclei can undergo a process of beta decay where the nucleus emits an electron and antineutrino resulting in the nucleus gaining a proton but losing a neutron [11].

$$(Z, N) \rightarrow (Z + 1, N - 1) + e^- + \bar{\nu}_e$$

In addition to the single beta decay described above, we can also have the process of double beta decay ($2\nu\beta\beta$). Here, two neutrons convert into two protons, emitting two electrons and antineutrinos.

$$(Z, A) \rightarrow (Z + 2, A) + 2e^- + 2\bar{\nu}_e$$

In unstable nuclei, $2\nu\beta\beta$ is negligible if single beta decay is possible. However, a specific set of unstable isotopes with even numbers of Z and N find themselves in a more energetically favorable state than their daughters. Therefore, the conservation of energy

ensures that specific transitions are forbidden, so it becomes more energetically favorable to undergo $2\nu\beta\beta$ to achieve a more stable configuration [7].

1.2.2 Neutrinoless Double Beta Decay ($0\nu\beta\beta$)

Neutrinoless Double Beta Decay is a theoretically predicted radioactive decay process yet to be observed. The process mirrors $2\nu\beta\beta$, except no neutrinos are emitted in the final state:

$$(Z, A) \rightarrow (Z + 2, A) + 2e^-$$

This decay process follows as a consequence of the neutrino being a Majorana particle, as the emission of two neutrinos in $2\nu\beta\beta$ could annihilate themselves resulting in none being observed.

Observing this phenomenon could have lasting implications. Specifically, it would mean that the lepton number is violated resulting in a possible explanation to the matter-antimatter asymmetry problem. [2]

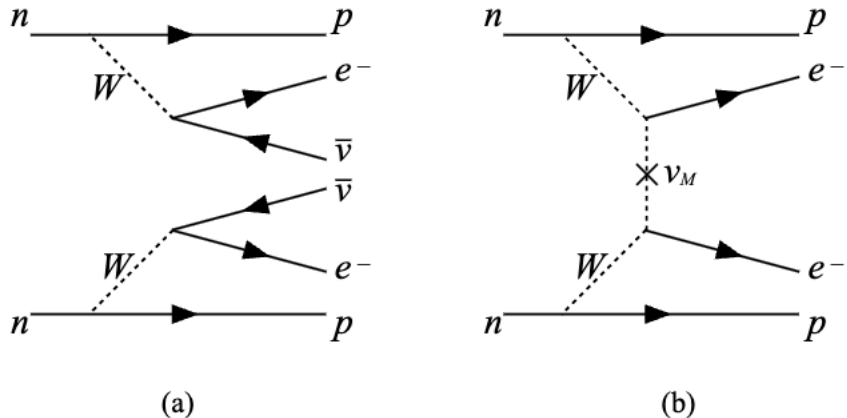


Figure 1.2: The Feynmann diagram for $2\nu\beta\beta$ (a) and it's theoretically predicted counterpart $0\nu\beta\beta$ (b) [7]. The latter assumes the model of light Majorana neutrino exchange.

1.3 Experimental Search for $0\nu\beta\beta$

There are two major ways to measure the two electrons that are emitted in $0\nu\beta\beta$: spectroscopy techniques and detectors capable of tracking and reconstructing the topology of

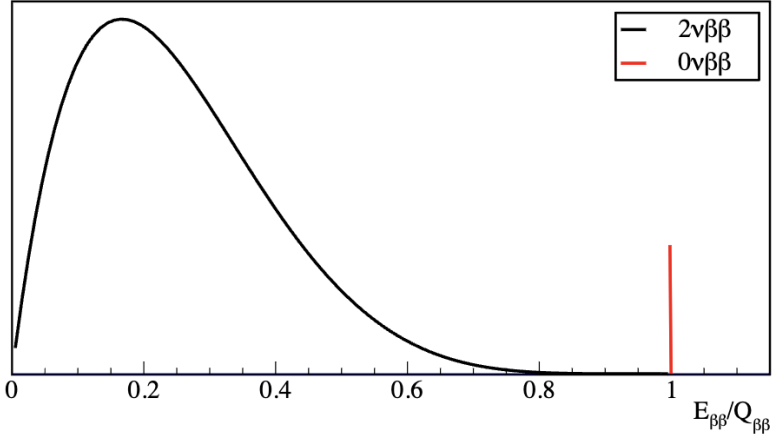


Figure 1.3: Theoretical $\beta\beta$ sum energy spectrum, ignoring background and detector effects which result in broadening of the $0\nu\beta\beta$ peak. Here the $0\nu\beta\beta$ peak has been artificially inflated to show behavior [7]

these electrons.

There are several possible candidates for $\beta\beta$ -decay; not all of them are suitable for such searches. The two main components for determining the suitability are the natural abundance and $Q_{\beta\beta}$ (double beta decay Q-value). In general, candidate $0\nu\beta\beta$ events are searched for in an energy regime around $Q_{\beta\beta}$ for each isotope, the number of events in this region is given by:

$$N \propto \frac{N_A a \epsilon M t}{W T_{\frac{1}{2}}} \quad (1.1)$$

In the above expression, N_A is Avogadro's number, W is the molar mass, a is the isotopic abundance, ϵ is the detector efficiency in the signal, M is the mass of the isotope, t is the measured time, and $T_{\frac{1}{2}}$ is the half-life of the isotope [5].

Eqn (1.1) is linearly dependent on the isotopic abundance. So for cases where the natural abundance is relatively high, such as ^{130}Te , we can directly use the natural element.

For these experiments, the energy resolution is critical as it allows us to distinguish $0\nu\beta\beta$ signal from the background resulting from natural radioactivity in the energy spectrum. Even if we were to create a background-free system, there would still be an expected background from $2\nu\beta\beta$ since the spectrum ends exactly at the position of the $0\nu\beta\beta$ signal (Fig 1.3). For an experiment with a non-negligible background, the sensitivity of S is

given by:

$$S \propto a\epsilon \sqrt{\frac{Mt}{B\Delta E}} \quad (1.2)$$

Here B is the background index and ΔE is the energy resolution. The goal of all $0\nu\beta\beta$ experimental searches is to optimize the above expression.

The $0\nu\beta\beta$ half life scales proportionally to $Q_{\beta\beta}^5$. Additionally, natural radioactivity limits the sensitivity of the experiment, so it becomes imperative to account for $Q_{\beta\beta}$ throughout these experiments.

There are several experimental techniques to help further account for these various issues and test for the existence of $0\nu\beta\beta$. In the next section, we shall be discussing one of these in greater detail [7].

CHAPTER 2

BACKGROUND INFORMATION

2.1 CUORE

The Cryogenic Underground Observatory of Rare Events (CUORE) is an experiment designed to search for $0\nu\beta\beta$ of ^{130}Te . CUORE is designed in the form of nineteen towers each containing thirteen floors of four crystals each, resulting in a close-packed array of 988 $5 \times 5 \times 5 \text{ cm}^3$, 750-g TeO_2 bolometers. Each floor has four TeO_2 crystalline detectors arranged in a 2×2 grid inside a copper frame equipped with an NTD (neutron-transmutation-doped) germanium thermistor that is continuously read out. The system operates inside a cryostat cooled to temperatures of $\sim 10 \text{ mK}$. The CUORE cryostat is located underground at the Gran Sasso National Laboratory in Italy in order to reduce extra background from incoming cosmic rays [5].

2.1.1 The CUORE Detector Setup

CUORE is entirely based on the TeO_2 crystalline bolometers. Specifically, the ^{130}Te isotope has been known to exhibit two-neutrino double beta decay ($2\nu\beta\beta$) and has a large natural abundance compared to other isotopes of interest (Fig 2.1). These crystals

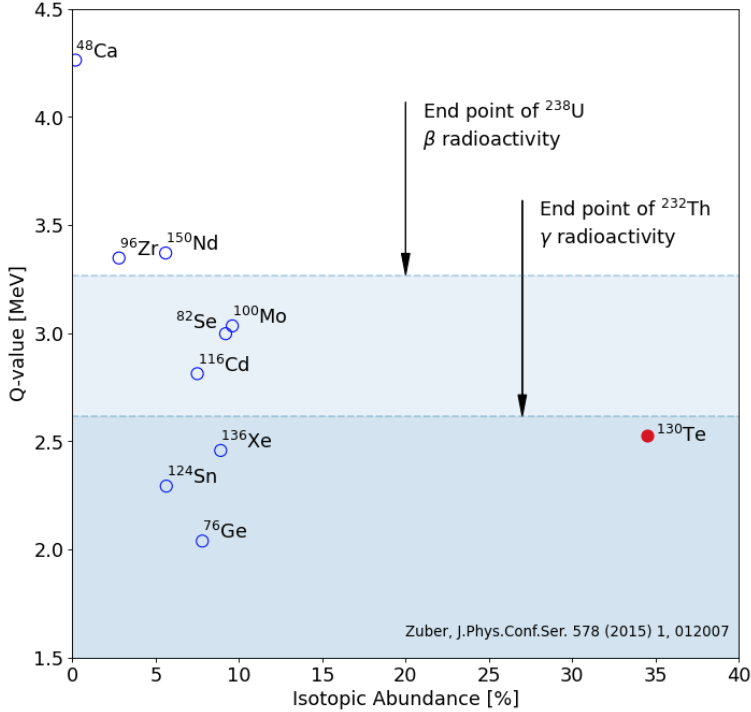


Figure 2.1: Common double beta decay isotopes, comparing natural abundance vs $0\nu\beta\beta$ Q-value. [13]

are specifically designed to be radio-pure. During assembly of the CUORE detector, they were stored in a nitrogen environment and a robotic arm was used to glue each of the NTDs to the crystal. Overall all these processes ensure that there is low intrinsic background and consistency amongst all the detectors.

CUORE's cryogenic calorimeters are designed to have low heat capacity at very low temperatures, resulting in a large change in temperature for any interaction with the lattice. Each time an energetic particle does so (for example, when a nucleus decays) it releases a small amount of heat. This is dispersed throughout the detector as phonons and the temperature change is registered on the Ge-NTD (Neutron Transmutation Doped) sensor, which functions as a resistive thermometer. That is, NTDs are designed such that their resistivity is very temperature-dependent, allowing for a good read-out of the temperature change after each decay. However, if these detectors were to function at room temperature this change would still be too small to properly detect. This is where the CUORE cryostat comes in to cool the sample down to mK temperatures ensuring a reasonable readout on the NTD devices [1]. A more detailed model of the CUORE

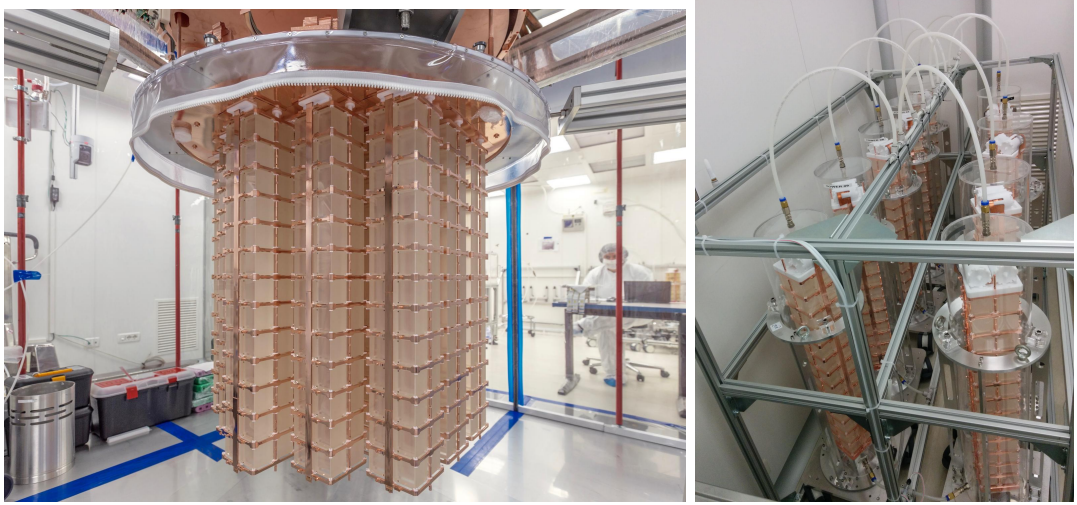


Figure 2.2: Fully assembled CUORE detector tower array (LEFT). The detectors being stored in a pure nitrogen environment (RIGHT) [4].

detector model is described in [3].

The CUORE dilution refrigerator is designed according to strict experimental requirements to be able to cool all of the detectors to approximately 10 mK. It accomplishes this by steadily cooling the system layer by layer with each one being colder than the previous [8].



Figure 2.3: Pictographic depiction of the CUORE cryostat [4].

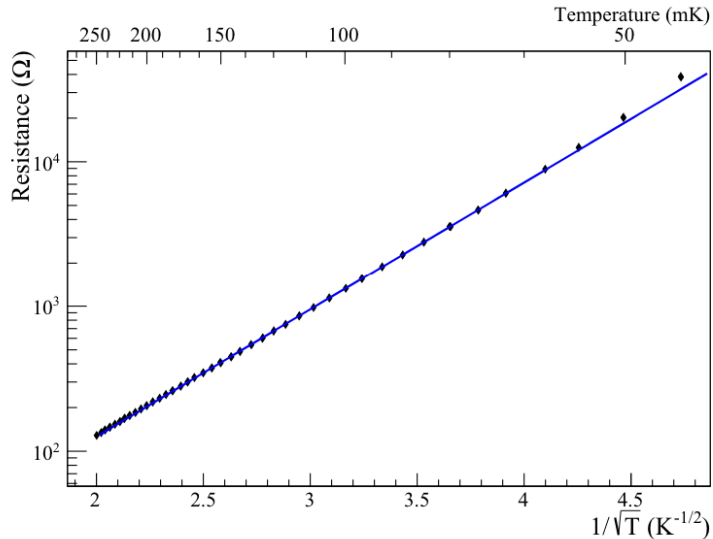


Figure 2.4: The resistance curve for a CUORE NTD [10]. The relationship between temperature and resistivity is given approximately by $R \propto \exp(1/\sqrt{T})$.

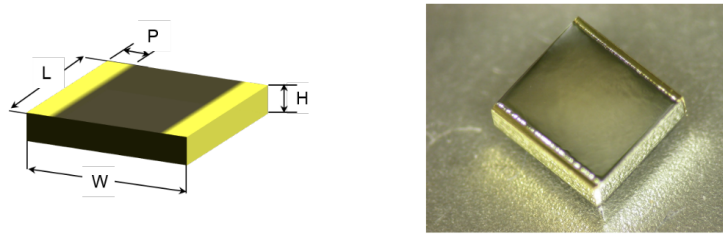


Figure 2.5: A CAD model of the CUORE NTD (LEFT). An image of the Ge NTD which is attached to each CUORE detector (RIGHT) [10].

2.1.2 Ge NTDs

As stated previously, each crystal is equipped with an NTD germanium sensor. Germanium is a semiconducting material. Via the process of neutron transmutation doping, Ge is doped to just below the metallic transition. At the low temperatures induced by the cryostat, the resistivity has an exponential temperature dependence

$$\rho(T) = \rho_0 e^{\sqrt{T_0/T}} \quad (2.1)$$

The constants $\rho_0 \sim 0.1 \Omega \cdot \text{cm}$ and $T_0 \sim 4 \text{ K}$ are determined by the doping level.

The relationship in Eqn 2.1 is what allows for the sensor to function as a resistive thermometer. The NTDs are located on the outside faces of each of the crystals facing the adjacent towers [10].

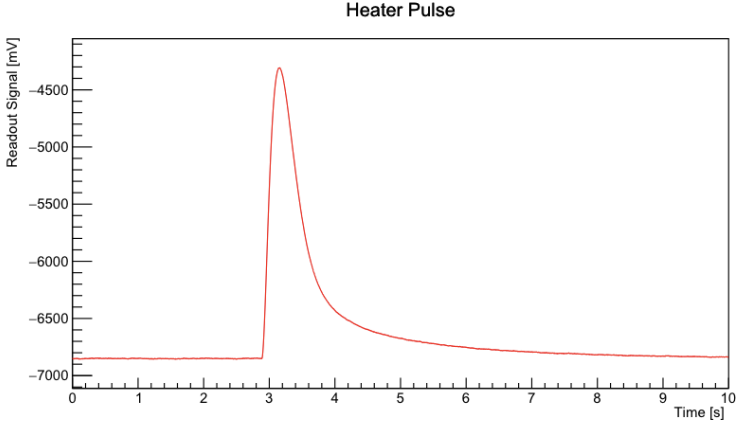


Figure 2.6: A sample of the CUORE pulse [9].

2.2 CUORE Data

2.2.1 Data Collection

The CUORE data is organized in runs which are grouped into data acquisition periods called datasets lasting 1-2 months. Different types of runs are performed depending on the use of the acquired data, for our purposes we are using calibration data. Calibration runs consist of $\mathcal{O}(1)$ day data acquisitions conducted in the presence of radioactive ^{232}Th gamma-ray emitting sources. Normally, the CUORE dataset has an initial calibration performed at the beginning of each dataset. This is followed by a month of background runs where data are acquired. Finally, the process terminates with another set of calibration runs. Each dataset would ideally be completed using the same operating conditions, however, changes in temperature or noise can potentially occur between datasets, so optimization runs are performed in between [6].

2.2.2 Calibration

CUORE distinguishes single particle pulses using two different software trigger algorithms. The data from the calibration runs are used to convert the Optimal Filter (OF) amplitudes into units of energy. During the calibration runs the detectors are exposed to radioactive Thorium and Cobalt sources, so the stabilized amplitudes of the γ lines are:

1. 511 keV: Created as a consequence of the positron-electron annihilation.

2. 1173 keV and 1333 keV: Consequence of the decay of ^{60}Co .
3. 2615 keV: Consequence of the decay of ^{208}Tl , from the ^{232}Th decay chain.

From here we obtain a collection of points to match the stabilized amplitudes to energies. This allows us to create a calibration function that converts the stabilized amplitude spectrum to an energy spectrum. For each crystal, a calibration function is of the form:

$$E = a_1 A + a_2 A^2 \quad (2.2)$$

The calibration coefficients, a_1 and a_2 are extracted on a channel-dataset basis, A is the stabilized amplitude of energy, and E is the energy [9].

The data that we are using for this analysis are from the 2-tonne year dataset, however, we are focusing on the 1-tonne-year data with the following cuts:

1. Total event energy in the range of 2590 keV - 2625 keV.

2. `MultipletValidation` is True

(this cut contains other cuts including `GoodForAnalysis==1`)

2.2.3 Energy Escape Events

Near (~ 1 cm) the surface of the TeO_2 crystal, if an energetic gamma ray were to interact with the crystal and produce a $e + e^-$ pair, two different energy escape events of interest could occur. First is a single escape; here one of the 511 keV gamma rays, from positron annihilation, escapes undetected by the primary crystal. This results in a peak at an energy of 511 keV less than the full-energy peak. The second is a double escape; here both 511 keV gamma rays escape undetected by the primary crystal and a peak will appear 1022 keV below the full-energy peak. The current understanding is that these events end up reconstructing relatively poorly, hence the goal of this project is to conduct a secondary analysis to improve the energy biases these create within the detectors. We are looking into the subset of events depicted in Fig 2.7.

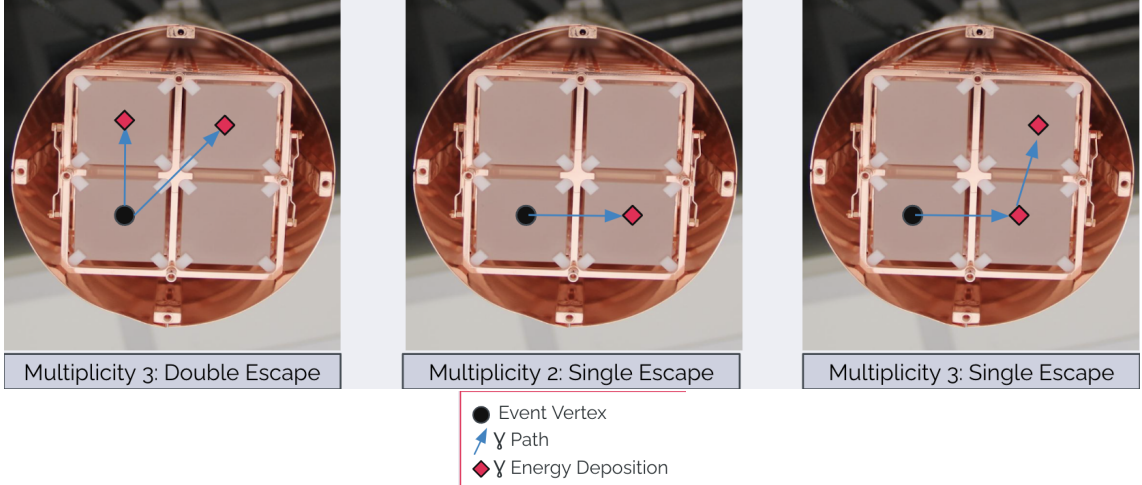


Figure 2.7: An illustration of the energy escape events discussed in this thesis.

2.2.4 Coincidence & Multiplicity

The cryogenic calorimetric detection method as used in CUORE precludes us from knowing the location of an interaction within any crystal. However, we can check if multiple crystals register the energy deposits simultaneously, this allows us to gain more information on the type of event. The main goal of coincidence analysis is to reject events with energy deposits in multiple crystals at once, removing a significant amount of background.

The multiplicity of an event is defined as the number of crystals that detect the energy deposition in coincidence with each other. The following factors are specified to determine coincidence:

- 1. Energy Threshold:** The minimum amount of energy to count as an ‘event’ in CUORE. The lower the threshold the more true coincidences can be caught. However, having it too low can result in the inclusion of random coincidences.
- 2. Distance:** The maximum distance between two crystals for them to be in coincidence. Correlated events will usually occur within crystals near each other.
- 3. Time Window:** The maximum amount of time between two events to count as a coincidence measurement. Since the timing resolution and accuracy of events are imperfect, a window must be chosen such that it’s wide enough to capture true coincidences while being small enough to ignore uncorrelated events.

For $0\nu\beta\beta$, we use an energy threshold of 40 keV with no distance limit and a time window of 5 ms. For coincidence cuts the energy threshold is 70 keV, a distance radius of 15 cm, and a time window of 150 ms. The distance cut ensures that the coincidence is only considered between a crystal and its immediate neighbors [9].

CHAPTER 3

CUORE DATA PRELIMINARIES & CHARACTERIZATION

3.1 Preliminaries

The goal of this project is to relate the topological relationships between high multiplicity events to energy biases present in their detection. So before any analysis, it becomes imperative to define the concept of topology. When a high multiplicity event occurs, energy is deposited in multiple different CUORE detectors within a close enough timescale and threshold. We discussed previously how these crystals are located close together, this allows us to define geometric relations between them. As a note, this is especially true for the events that we are discussing in this thesis (depicted in Fig 3.1).

There are four basic topologies for each primary crystal in relation to the position of the crystal detecting a second event: face, corner, edge, and none. Face, corner, and edge relationships are shown in Fig 3.1 and none is a broad category that encapsulates any topologies not included in the others. To prevent redundancy in the analysis, the primary crystal is always taken to be the one of largest energy depositions.

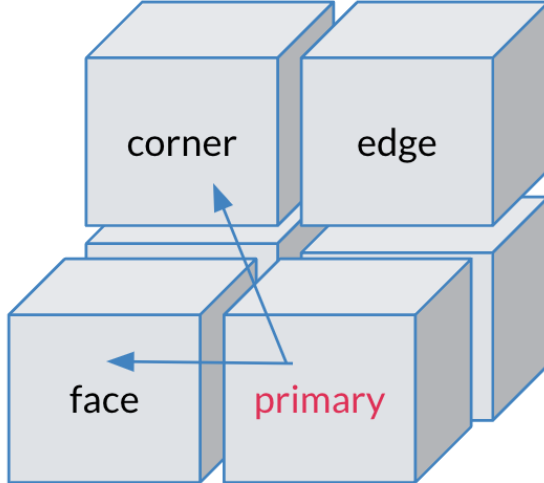


Figure 3.1: An illustration of the 3 major topologies (Face, Corner, and Edge) as they relate to the primary crystal. Here we also describe a complex topological energy event. The arrows represent the path of multiple high energy γ s as their energy is deposited from the primary crystal to the secondary ones.

For higher multiplicity (> 2) events these basic topologies are compounded to form more complex ones. An example of such a topology is shown in Fig 3.1. Here we describe a multiplicity 3 double escape event, we would describe this topology as Face-Corner (or Corner-Face, as the ordering is arbitrary in this algorithm).

3.1.1 Data Organization & Sorting

To start, data needed to be converted into an easily accessible format from its original ROOT files. We're working with data in the range of [2590, 2625] keV. I created a function that would convert all of the necessary components present in each file into a Pandas dataframe to be analyzed with Python. From here, we had to understand how crystals in multiple-deposit events were related to each other in position space. Using the known lists of various face, edge, and corner neighbors of each crystal I created a sorting algorithm that could determine the topological relationships of every crystal.

Total energy of event – should sum to ~ 2615 keV since the data is for the ^{232}Th calibration line	Individual energy caught by the NTDs of each crystal present in the event.	Crystals present in each event
Dataset Run Channel Tower Layer EventTime Energy TotalEnergy Multiplicity	Energy ChannelV	DeltaTV MultipletValidation OrderInMultiple Neighbors
1 3601 350359 148 3 2 1494556128264 2338.517514 2618.587818 2 [2338.517514453725, 280.0703039670164] [148, 147] [0.0, -5.4388387070503086e-05] True 2 [S, F148]		

Primary crystal → usually taken to be one of largest energy deposition

Number of crystals engaging in each event

Figure 3.2: A single row of the pandas dataframe describing a multiplicity 2 single escape event. The last column was added independently to describe the various topologies.

A single row of the pandas dataframe is shown in Fig. 3.2. The last column is a consequence of the sorting algorithm. In the figure above, the primary crystal is taken to be 148 since it has the largest energy deposition. The second crystal present is a face neighbor of 148 (F148).

3.1.2 Two-Dimensional Histograms

Starting with the events of multiplicity 2 and 3, I plotted the relationships between energies to search for patterns. There were a variety of plots for each topology, but they revealed similar results as the following showcased in Fig 3.4.

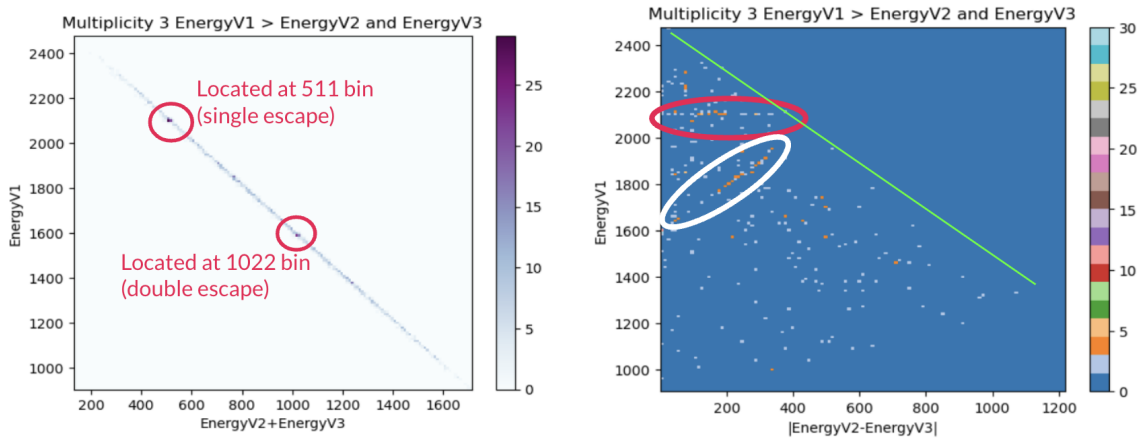


Figure 3.3: Two-dimensional histograms for all multiplicity 3 events.
RIGHT: The energy deposited in the primary crystal (EnergyV1) vs the sum of the energy deposited in the two secondary crystals (EnergyV2+EnergyV3).
LEFT: The energy deposited in the primary crystal (EnergyV1) vs the absolute difference of the energy deposited in the two secondary crystals (EnergyV2-EnergyV3)

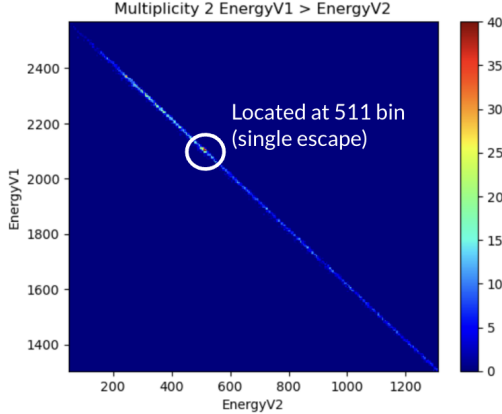


Figure 3.4: Two-dimensional histograms for all multiplicity 2 events. The energy deposited in the primary crystal (EnergyV1) vs. the energy deposited in the secondary crystal (EnergyV2).

The linear behavior of the summation of both multiplicity 3 and 2 events, is a result of energy conservation since all the depositions must sum to 2615 keV. Consequently, all of the energy in the difference is below the green line which defines the same 2615 keV total energy. In general, we can see a high density of single and double escape events, implying that such events occur in larger numbers than what was previously assumed.

Specifically, there are some interesting striations present in the multiplicity 3 energy difference plots. These trends are highlighted in red and white. Specifically, the red which we extract and analyze later is correlated to the single escape peaks where the energy deposited in the primary crystal is 2104 keV and the energy deposited in the other crystals sums to 511 keV.

3.1.3 A Dabble into PCA

Principle Component Analysis (PCA) is a data analysis method where a dataset with high dimensionality is reduced. The process works by transforming a large number of correlated variables into a smaller set of principle components via a vector space transformation. There is an emphasis on variations present in the dataset and strong patterns in the data set are brought forward. The principle components are uncorrelated and ordered such that the first few carry most of the variational information about the dataset. From here the data points can be graphed in this reduced space with the basis vectors being

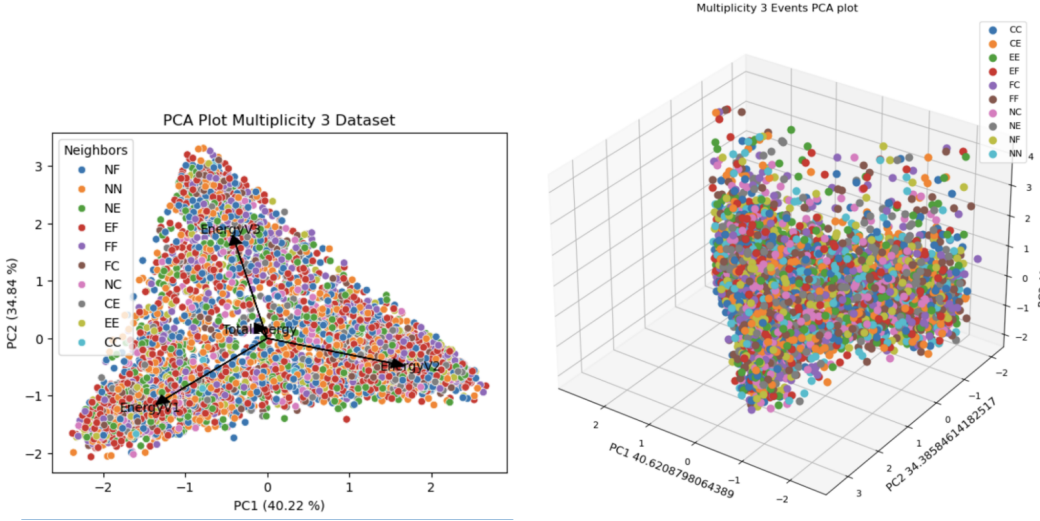


Figure 3.5: The PCA plots for various topologies in the multiplicity 3 events. Each topology is simplified i.e. FN (Face-None). RIGHT: Two-dimensional plot with the principle component vectors. LEFT: Three-dimensional plot.

the PCA components and possible trends can be analyzed.

Several variations of PCA analysis were conducted on our datasets. We attempted to isolate double vs single energy escape events and added different variables to find correlations. However, this analysis was largely uninformative, and we saw a uniform distribution of all topologies (shown for multiplicity 3 in Fig 3.5). The conclusion was that PCA continues to function properly, but needs a stricter dataset to work with to see the topological relations.

3.1.4 Box Plots

PCA informed us that there wasn't a large topological dependence on the energy reconstruction. To confirm our hypothesis that there was indeed a topological component present, we proceeded to create box plots of the various multiplicity events to view any possible deviations.

In general, there seems to be a shift in the box plots across different topologies and different events, implying that a topological element is indeed present.

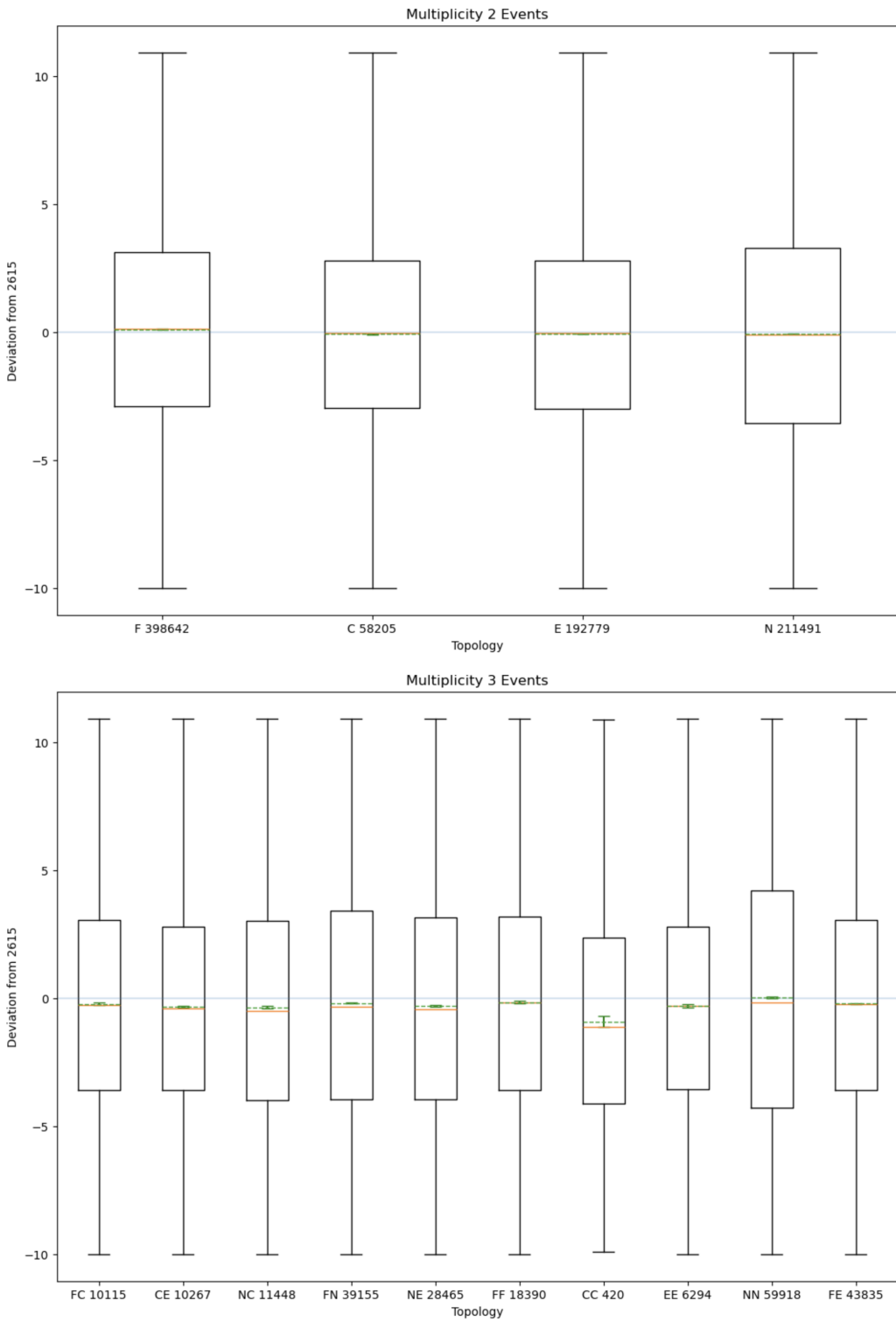


Figure 3.6: Box plots of the deviations from 2615 keV of the total energy for multiplicity 2 (TOP) and multiplicity 3 (BOTTOM) events upon the removal of the events with deviations greater than 20 keV.

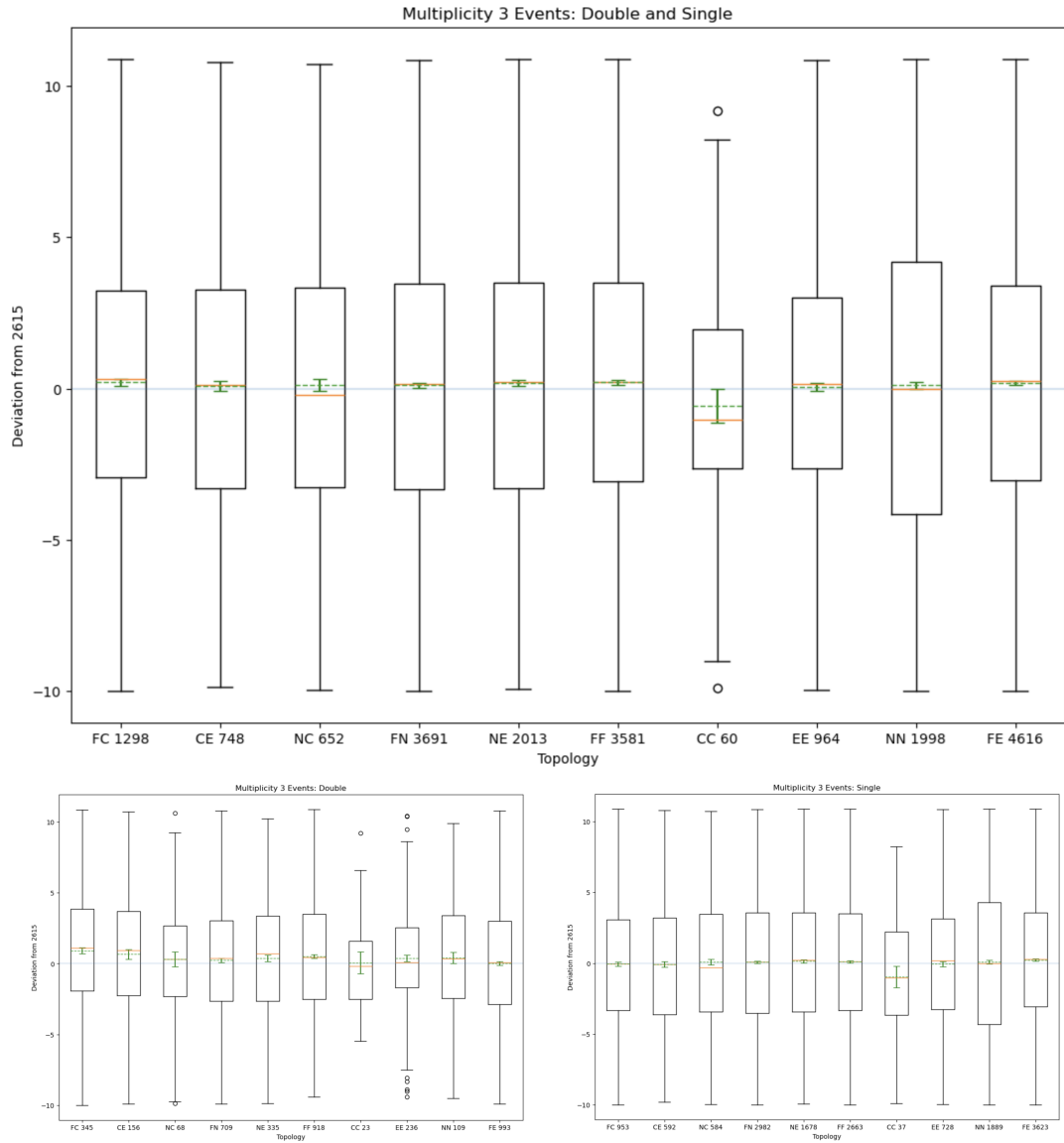


Figure 3.7: Multiplicity 3 single and double escape event box plots.

3.2 Gaussian Fits

Since PCA wasn't a fruitful way to understand how energy reconstruction is topologically dependent, but the box plots do show some level of dependence, we moved to attempt a more manual analysis technique. Specifically, we divided the events into their single and double escape subsets and proceeded to individually fit each topology with a Gaussian to extract the peak shape parameters. The overarching goal here was to further isolate the topologies that are problematic.

3.2.1 Single Escape Events

The single escape energy events were extracted by bounding the energy deposited in the primary crystal to be between [2070, 2130] keV. The 2100 keV energy distribution was fit using a Gaussian with linear background. Initially, the 511 keV energy fits were poor due to the non-linear background. To simplify this we proceeded to extract the standard deviation from the 2104 keV fits of the same topology, denoted as σ_{2104} . From here we proceeded to only take events within $\pm\sigma_{2104}$ of the 511 keV peak.

Multiplicity 3

The Gaussian fits for both the 2100 keV and 511 keV energy distributions are depicted in Fig 3.9 and Fig 3.8, respectively. The mean and standard deviations extracted from each of these fits are shown in Fig 3.10 for each topology. The only missing topology is corner-corner, the main reason for this was because the fits were very unreliable due to incredibly low statistics.

There seems to be a large discrepancy between the extracted means and the expected value of 511 keV, so we refit the data upon removing the non-linear background. These reduced background 511 keV fits are shown in Fig 3.11 with their corresponding extracted parameters shown in Fig 3.12.

When a Gaussian fit with a linear background is applied to the reduced 511 keV energy distribution, the extracted parameters become much more consistent with the expected. However, there still seems to be some level of discrepancy present where most of the topologies are still closer to ~ 510 keV than 511 keV. It seems the topological relations of the NTD with respect to other crystals plays a larger role in energy decomposition than we had initially assumed. So the task now is to determine face-neighbor topologies of the NTDs in each crystal and correlate energy discrepancies with this characterization.

Additionally, when we proceeded to analyze the energy deposited in the primary crystal with the 2100 keV fits, there seemed to be statistically significant deviations. This further supports our hypothesis that the location of the event vertex seems to affect the energy decomposition, as different topologies have very different results from one

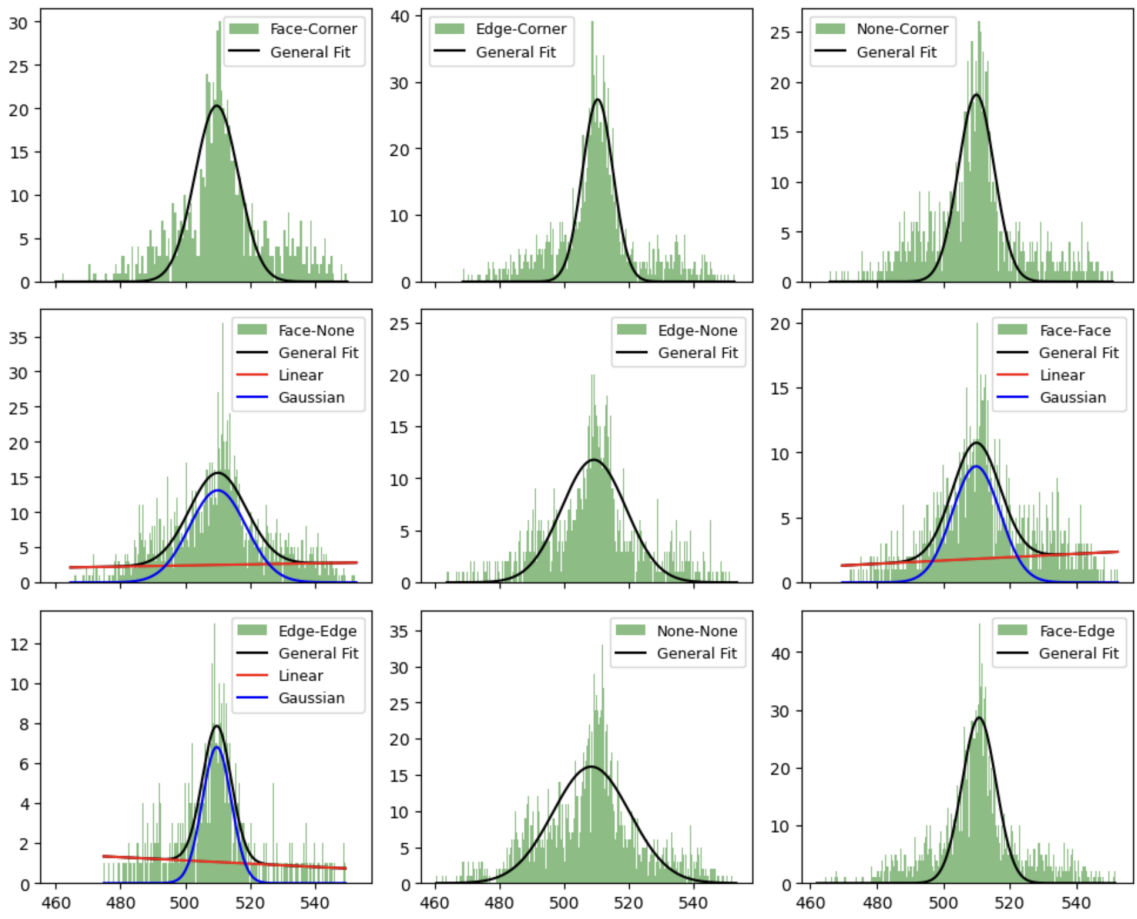


Figure 3.8: The 511 keV energy distribution Gaussian fits with the present non-linear background.

another. The next step in this process was to correlate what we had found here with the NTD topologies of each crystal.

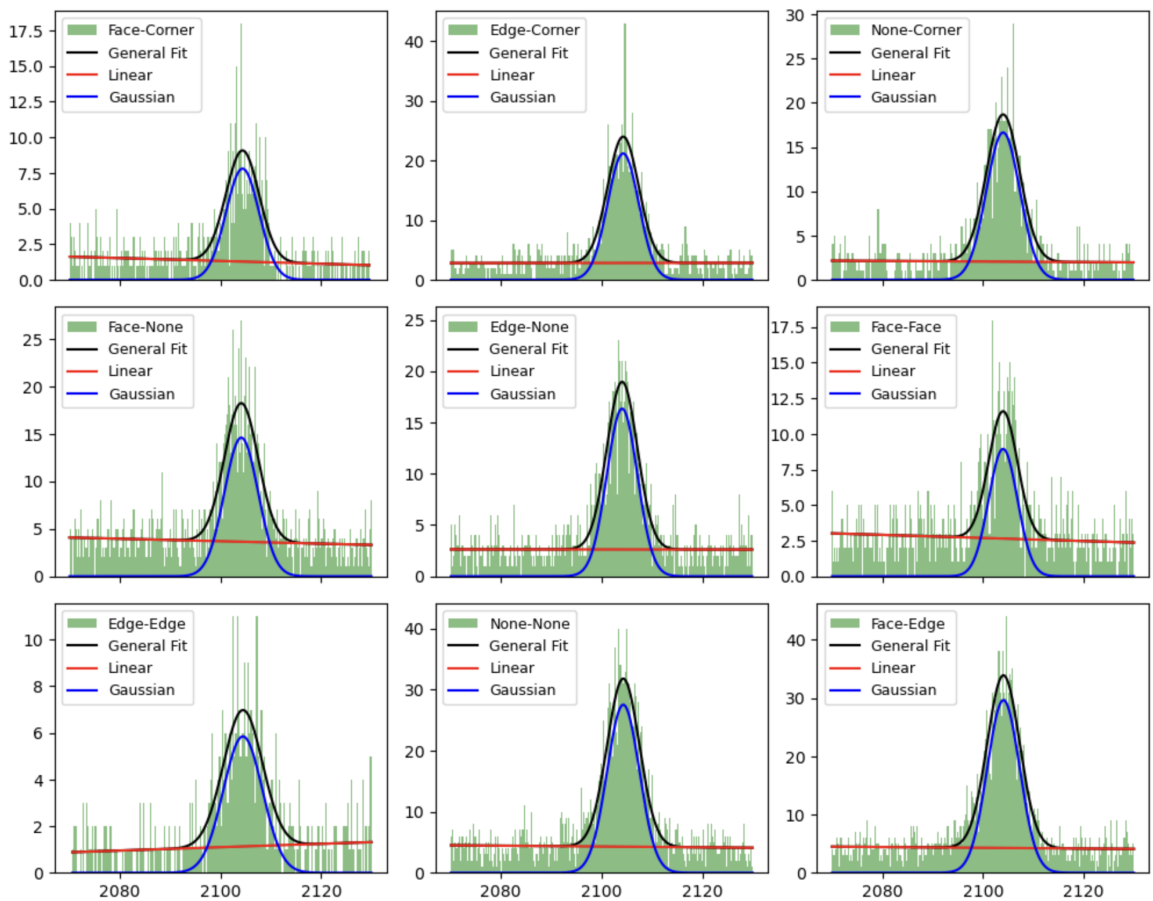


Figure 3.9: The 2100 keV energy distribution Gaussian fits with linear background.

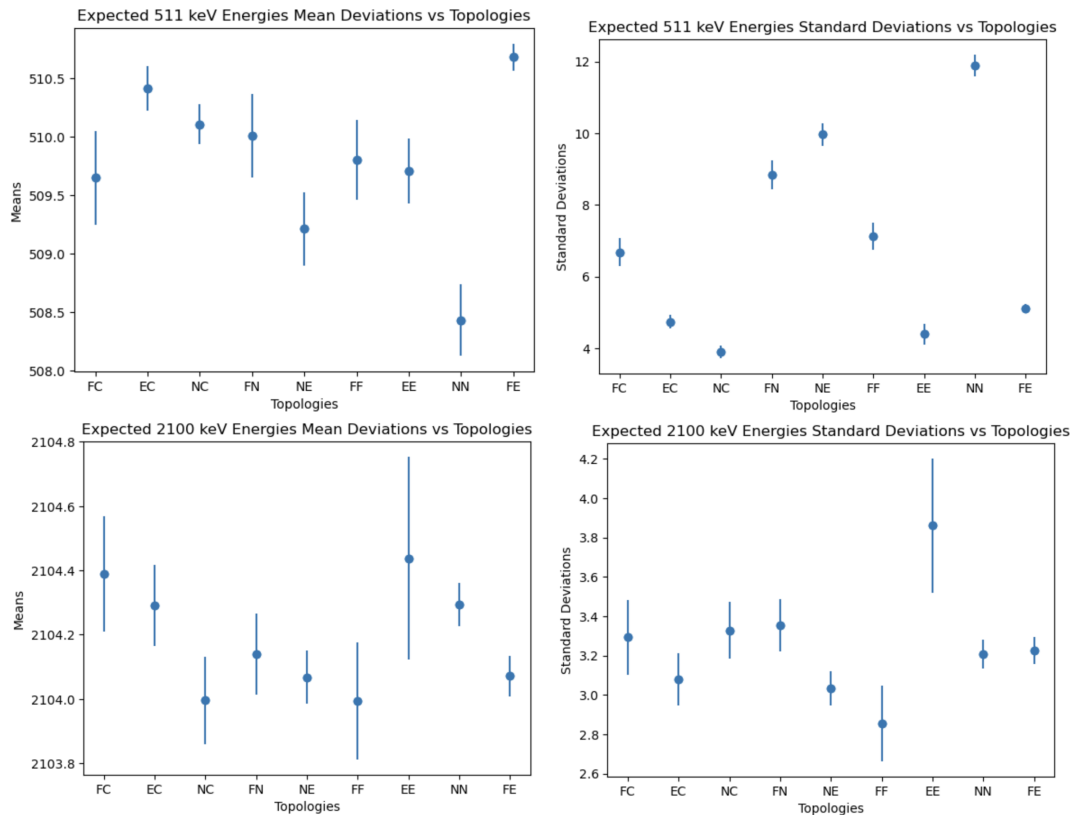


Figure 3.10: The extracted mean and standard deviations of the 511 keV and 2100 keV energy distributions with their corresponding error shown in Fig 3.9 and Fig. 3.8.

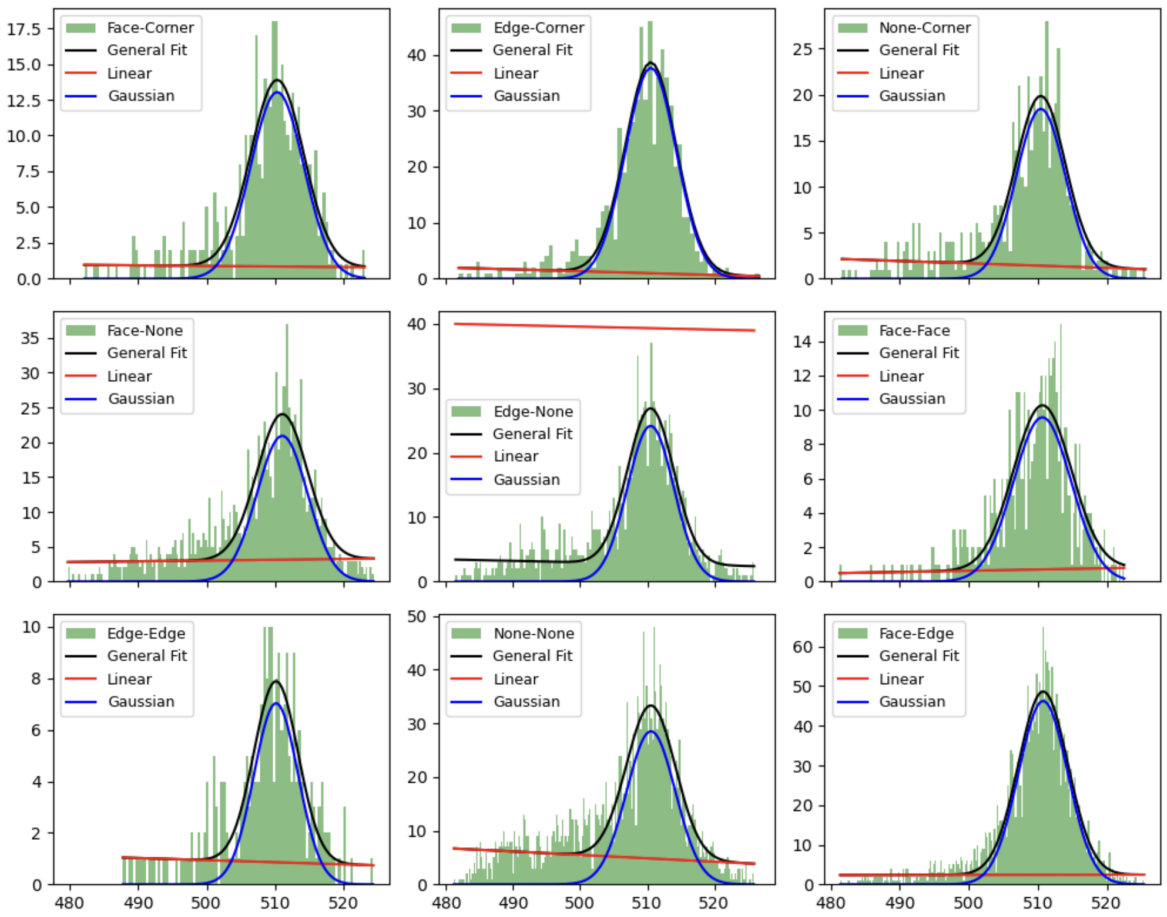


Figure 3.11: Gaussian fits with linear background for the 511 keV energy distribution. We restricted to events within $\pm\sigma_{2104}$ to remove the non-linear background.

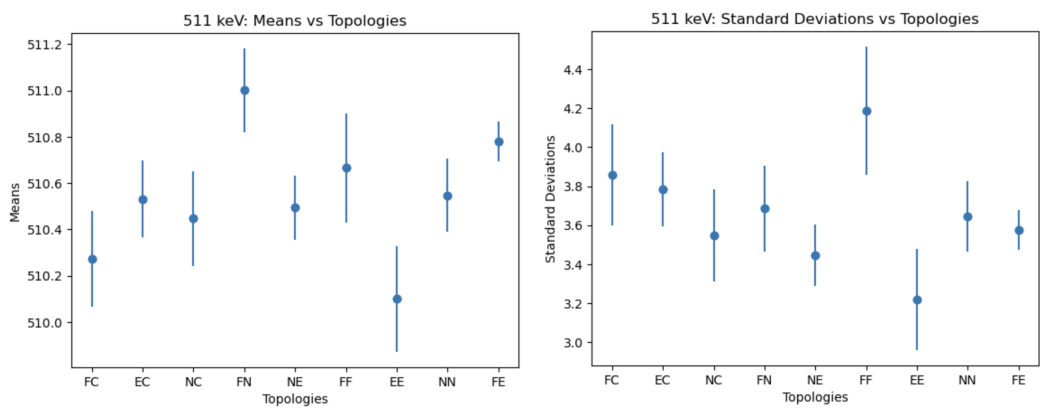


Figure 3.12: The extracted mean and standard deviations of the 511 keV energy distributions with the reduced background shown in Fig. 3.11, and their corresponding error.

CHAPTER 4

NTD TOPOLOGY ANALYSIS

We begin by defining the concept of an NTD event. Specifically, all of the higher multiplicity events can be divided into two large categories:

1. Same Tower Events: These events occur within one of the CUORE towers. Since the NTDs are located on the outside faces of each crystalline tower, these types of events don't cross NTD faces.
2. Across Tower Events: These events cross the CUORE towers and consist of both NTD events and no NTD events depending on which crystal face an NTD is located.

In general, we focus on the across-tower events that cross NTD faces. Here the NTDs located on the two across-tower crystal neighbors are facing each other. Therefore if an energetic particle follows this path, it ends up crossing two NTDs. Clearly, the events with NTDs occur near the surface of each detector and are the minority when compared to the statistics of the No NTD events. The goal is to compare these with events that don't have this NTD topology.

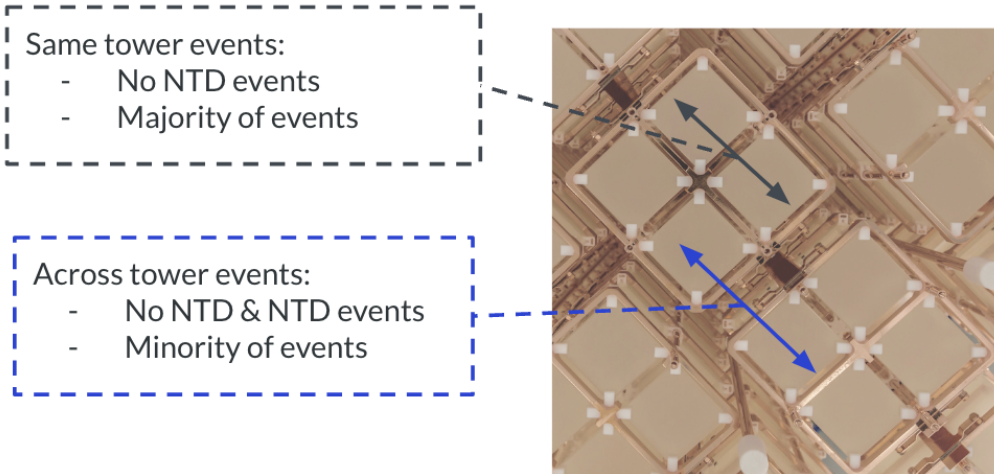


Figure 4.1: A pictographic representation of the two types of tower events.

4.1 Single Escape Events

After dividing the events into NTD and no-NTD categories, the goal was to fit Gaussians to these energy distributions. However, there was a severe non-linear background present in the 511 keV distribution. To start, for the multiplicity 3 events, we attempted a similar approach as described previously, where we assumed that $\pm 4\sigma_{2104}$ outside the 2100 keV peak was considered background. From here we proceeded to graph the 511 keV energy distribution in this range. The expectation was that this 511 keV background would be Gaussian or exponential. However, we found it was a double Gaussian or polynomial. This odd behavior of the background was the consequence of the sum of the smaller energies being correlated and/or anti-correlated to the higher energy. The conclusion was to condense the events to the range of [490, 540] keV and fit this reduced distribution with an exponential background and Gaussian. Additionally, most of the topological analysis happens for the No-NTD Face events since those have decent statistics for us to analyze.

4.1.1 Multiplicity 2

Due to the setup of the CUORE towers, for all of the multiplicity 2 NTD events the primary and secondary crystals are face neighbors. However, we can proceed to analyze the topologies of the No NTD events. The fits for these events were slightly different than

those of multiplicity 3. The main addition was a Gaussian error function or smeared step function at the mean value. In general, we continue to see differences in the various topologies, however, these values still remain relatively consistent with the 511 keV Gaussian mean expectation. However, there does seem to be a deviation present between the 511 keV energy reconstructions over different topologies.

Additionally, we also proceeded to continue this analysis for the energy deposited inside the primary crystal. The fits conducted here were a Gaussian with a linear background. Overall, we continued to see consistency between the expected energy reconstruction of the 2104 keV peak for both the Non-NTD Face and NTD Face events.

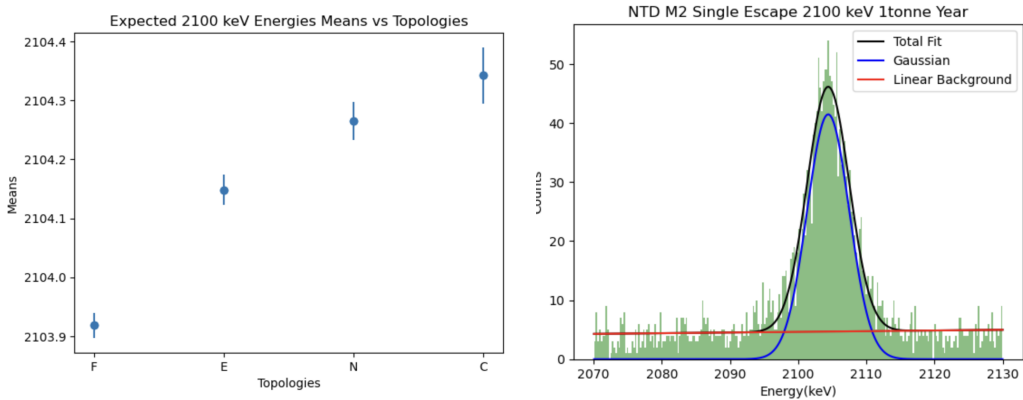


Figure 4.2: Summary of the extracted mean values and their corresponding errors for the various topologies in the multiplicity 2 primary crystal energy distribution for Non-NTD Face events (LEFT). Gaussian fit for the NTD Face events with its mean and standard deviation labeled (RIGHT).

Topology	Mean (keV)	Standard Deviation (keV)
Non-NTD Face	2103.92 ± 0.02	3.18 ± 0.022
Non-NTD Corner	2104.34 ± 0.047	3.09 ± 0.05
Non-NTD Edge	2104.15 ± 0.026	3.12 ± 0.027
Non-NTD None	2104.27 ± 0.032	3.18 ± 0.034
NTD	2104.4 ± 0.06	3.09 ± 0.07

Table 4.1: The mean and standard deviation of the Gaussian fits for the multiplicity 2 Non-NTD Face primary crystal energy distribution.

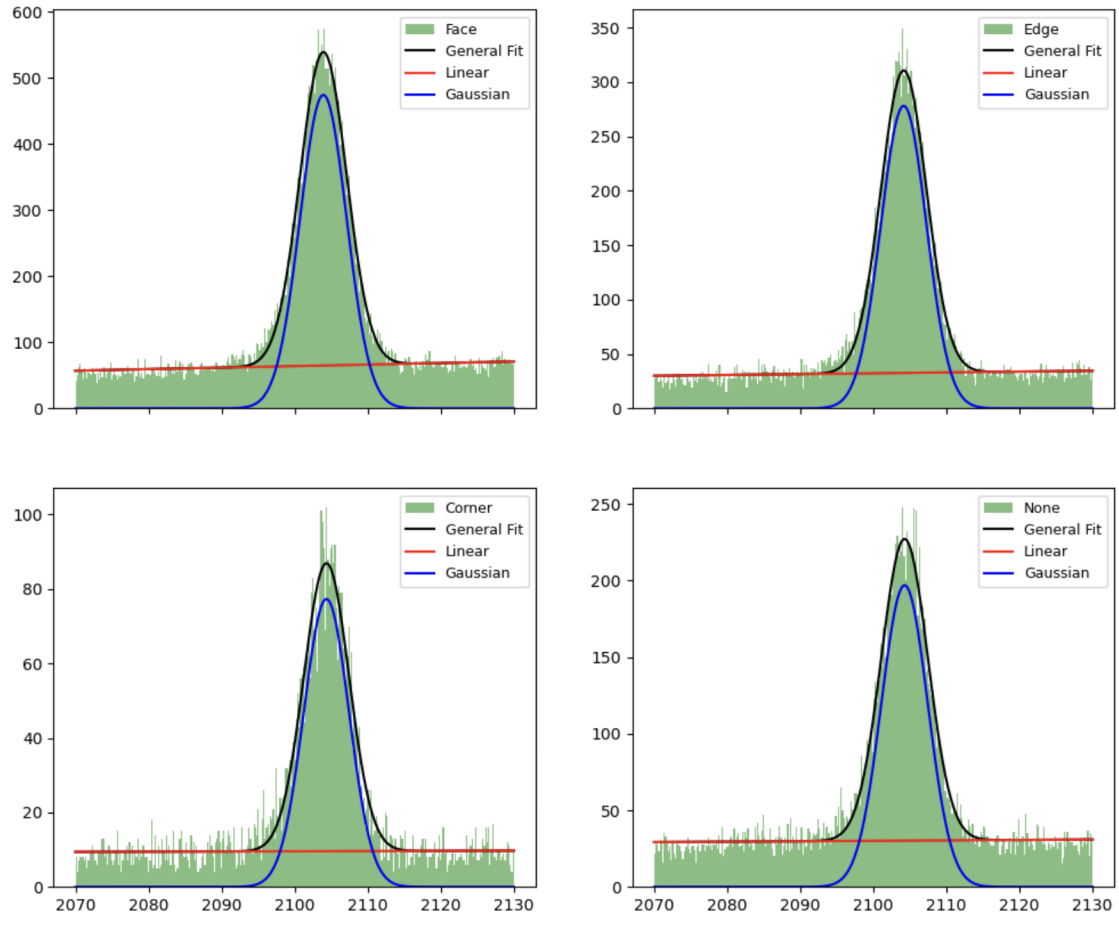


Figure 4.3: Gaussian fits for multiplicity 2 single escape events in the primary crystal for the various topologies in the Non-NTD Face dataset.

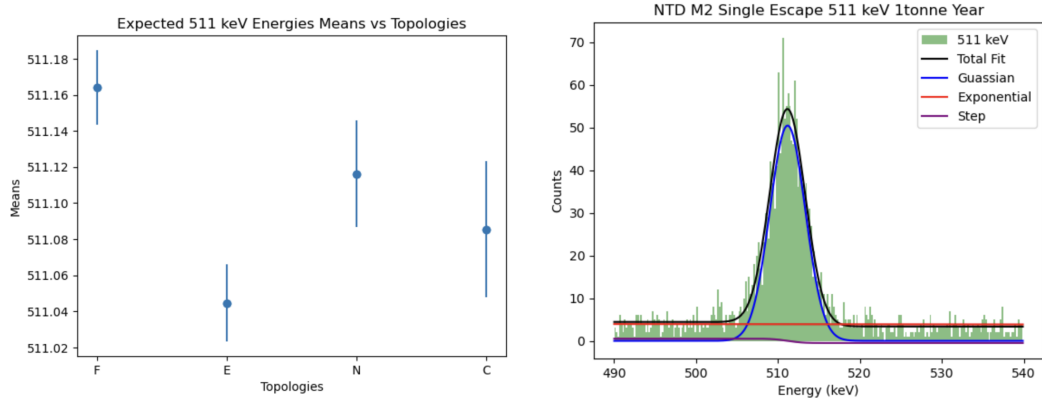


Figure 4.5: Summary of the extracted means for the various topologies in the Non-NTD Face multiplicity 2 dataset (LEFT). The Gaussian fit for the NTD Face events for multiplicity 2 (RIGHT).

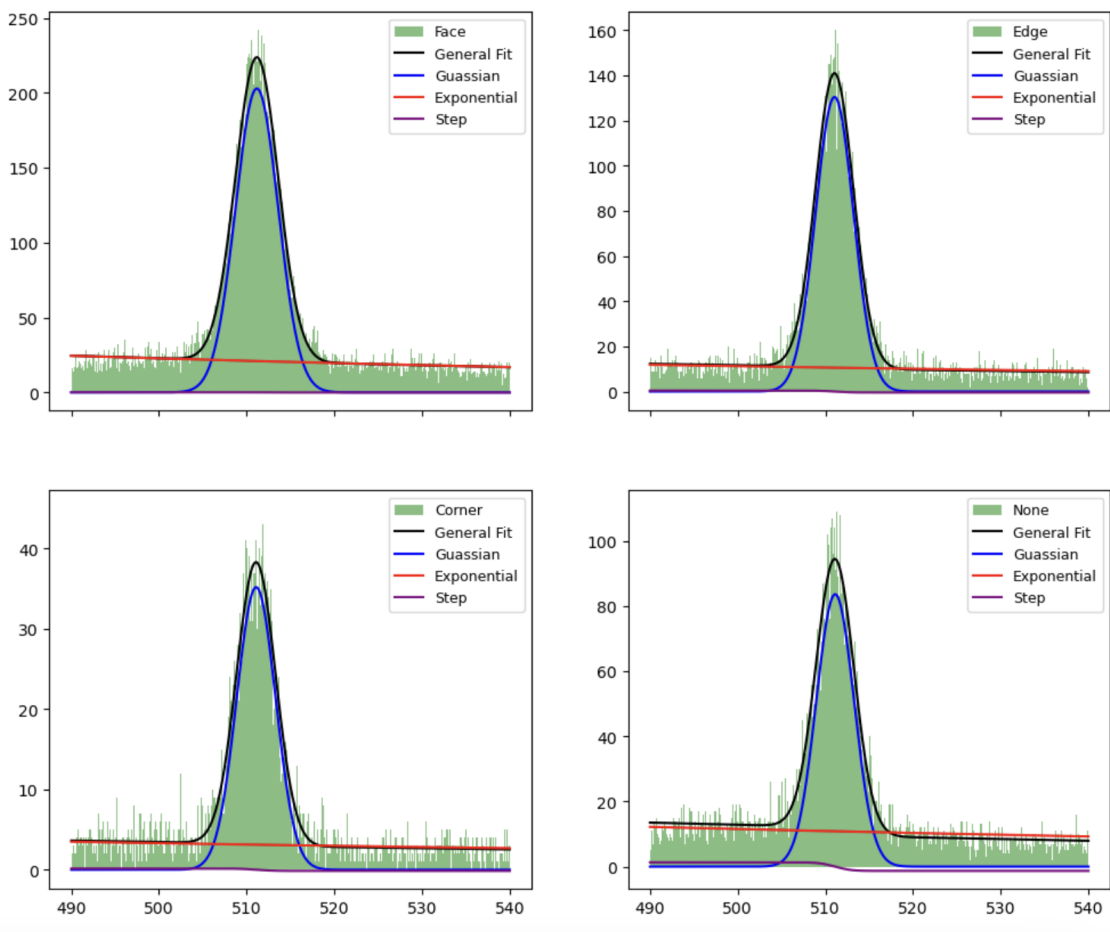


Figure 4.4: Gaussian fits for multiplicity 2 single escape events in the secondary crystal for the various topologies in the Non-NTD Face dataset.

Topology	Mean (keV)	Standard Deviation (keV)
Non-NTD Face	511.16 ± 0.02	2.44 ± 0.01
Non-NTD Edge	511.04 ± 0.02	2.16 ± 0.02
Non-NTD Corner	511.09 ± 0.04	2.22 ± 0.03
Non-NTD None	511.12 ± 0.029	2.16 ± 0.02
NTD	511.18 ± 0.02	2.16 ± 0.015

Table 4.2: The mean and standard deviation of the Gaussian fits for the multiplicity 2 Non-NTD Face secondary crystal energy distribution.

4.1.2 Multiplicity 3

The analysis described in the previous section was repeated for the multiplicity 3 single escape events, with the only defining difference being that the fits didn't include the

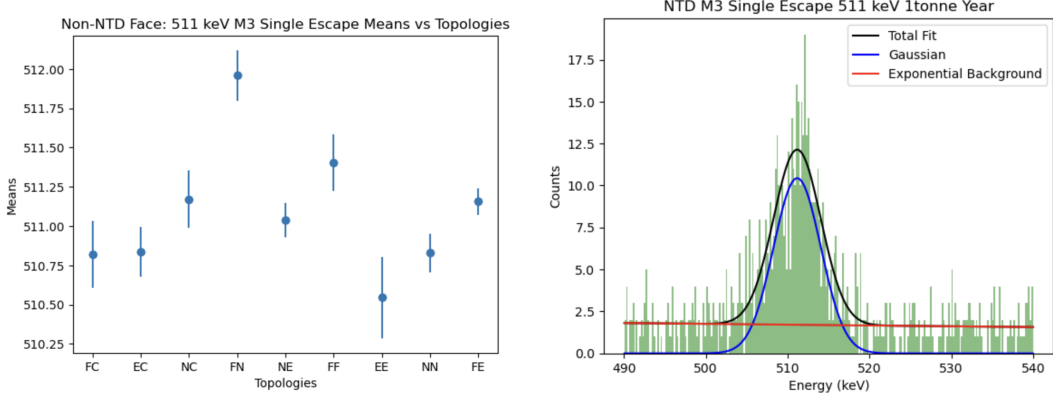


Figure 4.7: Summary of the extracted mean values and their corresponding errors for the various topologies in the multiplicity 3 primary crystals for Non-NTD Face events (LEFT) and the NTD Face events Gaussian fit (RIGHT).

addition of a smeared Gaussian error function. In general, we found similar results, as described in the previous section. The main idea to note here is that there seems to be more consistency within the Non-NTD and NTD 2100 keV fits than what was seen in 3.10. However, we still continue to see deviations present in the 511 keV and 2104 keV energy reconstruction.

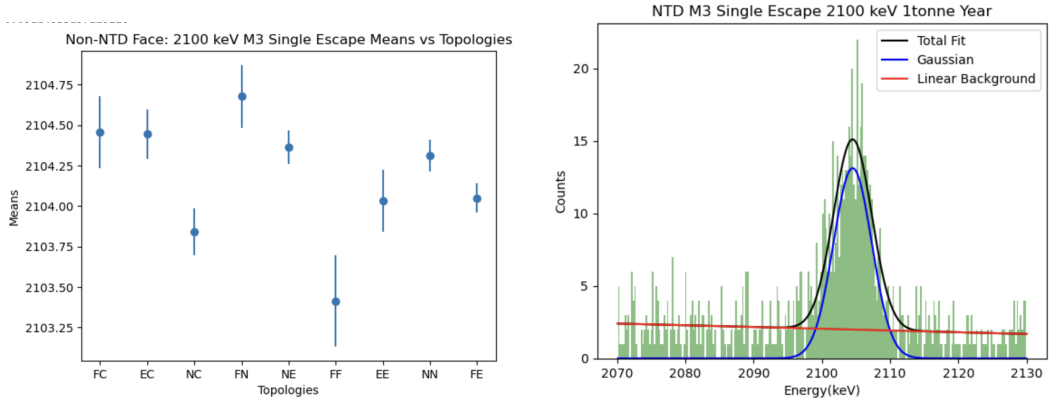


Figure 4.6: Summary of the extracted mean values and their corresponding errors for the various topologies in the multiplicity 3 primary crystals for Non-NTD Face events (LEFT) and the NTD Face events Gaussian fit (RIGHT).

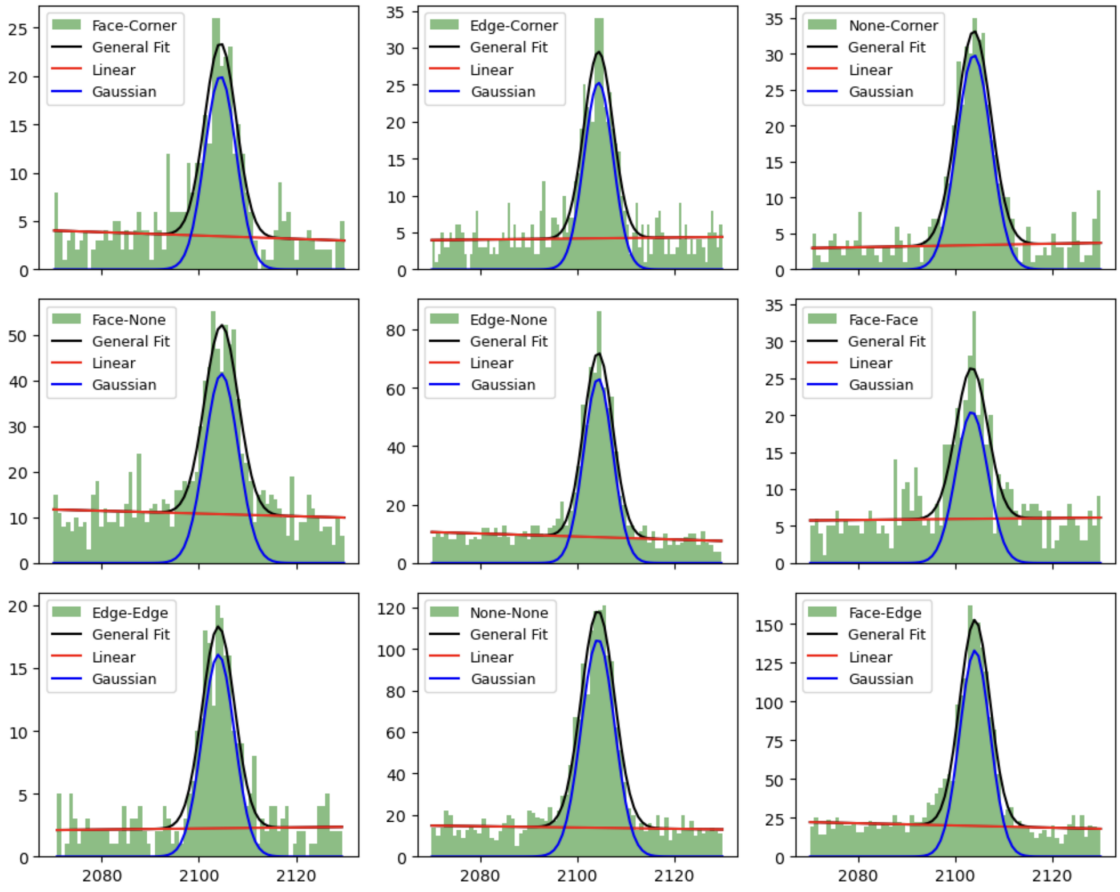


Figure 4.8: Multiplicity 3 Gaussian fits for energy deposition inside the primary crystal in the Non-NTD Face dataset over various topologies.

Topology	Mean (keV)	Standard Deviation (keV)
Non-NTD Corner-Edge	2104.44 ± 0.15	2.94 ± 0.16
Non-NTD Face-Corner	2104.46 ± 0.22	3.26 ± 0.24
Non-NTD None-Corner	2103.84 ± 0.15	3.54 ± 0.15
Non-NTD Edge-Edge	2104.03 ± 0.19	3.33 ± 0.20
Non-NTD None-Edge	2104.36 ± 0.01	2.99 ± 0.11
Non-NTD Face-Face	2103.41 ± 0.28	3.29 ± 0.3
Non-NTD None-None	2104.31 ± 0.1	3.42 ± 0.1
Non-NTD Face-Edge	2104.05 ± 0.09	3.13 ± 0.1
Non-NTD Face-None	2104.68 ± 0.19	3.46 ± 0.21
NTD-Face	2104.50 ± 0.128	2.81 ± 0.13

Table 4.3: The mean and standard deviation of the Gaussian fits for the multiplicity 3 Non-NTD Face primary crystal energy distribution.

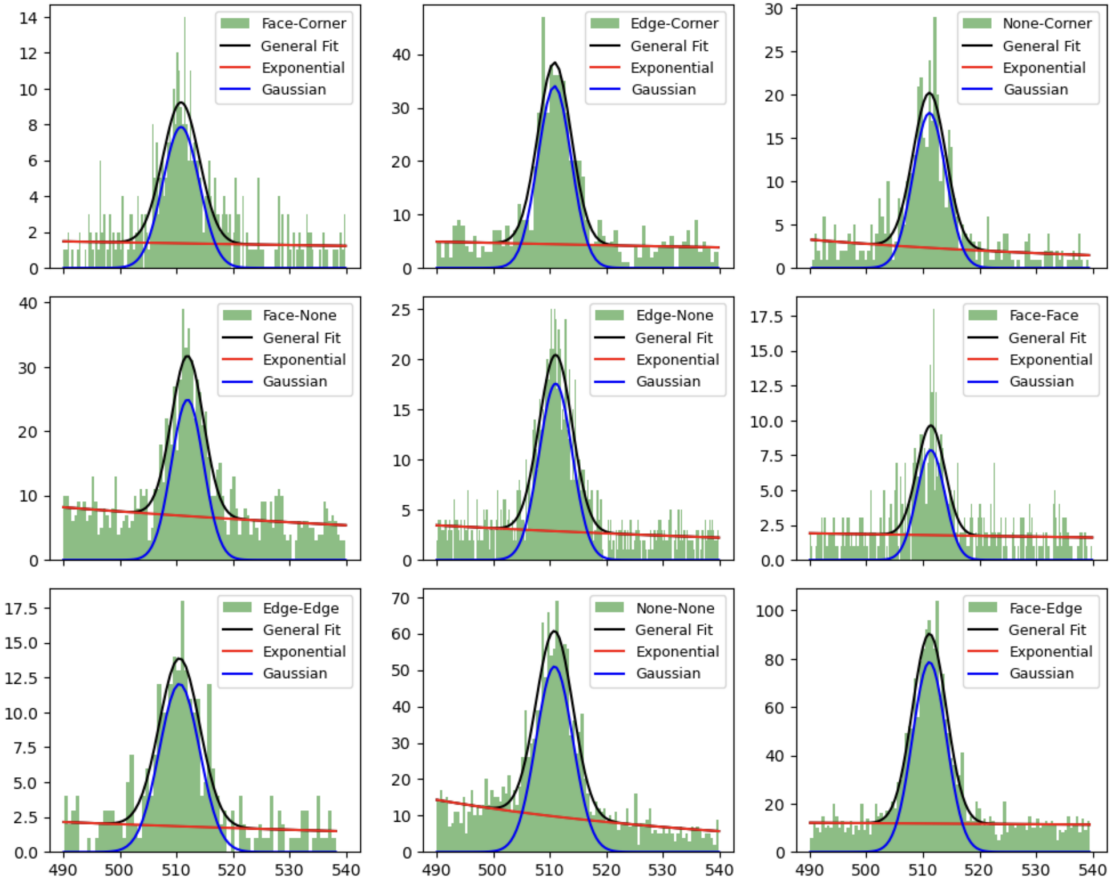


Figure 4.9: Multiplicity 3 Gaussian fits for energy deposition inside the secondary crystals in the No-NTD Face dataset over various topologies.

Topology	Mean (keV)	Standard Deviation (keV)
Non-NTD Corner-Edge	510.83 ± 0.16	2.94 ± 0.17
Non-NTD Face-Corner	510.82 ± 0.21	3.23 ± 0.23
Non-NTD None-Corner	511.17 ± 0.18	2.90 ± 0.19
Non-NTD None-Edge	511.03 ± 0.11	2.93 ± 0.12
Non-NTD Face-Face	511.4 ± 0.18	2.46 ± 0.19
Non-NTD Edge-Edge	510.54 ± 0.26	3.57 ± 0.28
Non-NTD None-None	510.83 ± 0.12	3.25 ± 0.13
Non-NTD Face-Edge	511.16 ± 0.09	2.99 ± 0.1
Non-NTD Face-None	511.96 ± 0.16	2.83 ± 0.17
NTD-Face	511.16 ± 0.14	2.89 ± 0.15

Table 4.4: The mean and standard deviation of the Gaussian fits for the multiplicity 3 Non-NTD Face secondary crystal energy distribution. The last row shows the NTD-Face event values.

4.2 Lineshape Analysis

The next step was to compare the Non-NTD Face and NTD Face topologies over each dataset and to the expected calibration line for the multiplicity 3 single escape events. The expected data points were extracted from the calibration lineshape and residuals of the CUORE detectors for each dataset. The main thing to note is that there are clear variations present both between the Non-NTD Face and NTD Face events as well as how these compare to the expected calibrated points. These lineshape calibration points were obtained from CUORE internal documentation.

Due to these variations, it's becoming clear that the process of conducting these calibrations doesn't take into consideration the wide deviations that are present for these various topologically different events. An important note to make is that the statistics for the fits conducted per dataset are quite low, especially for the NTD Face events, therefore it becomes important to repeat this analysis when the full two-tonne year data is accessible for better validation of these results. However, regardless of the low statistics, the results we're seeing are indicative of the biases discussed previously.

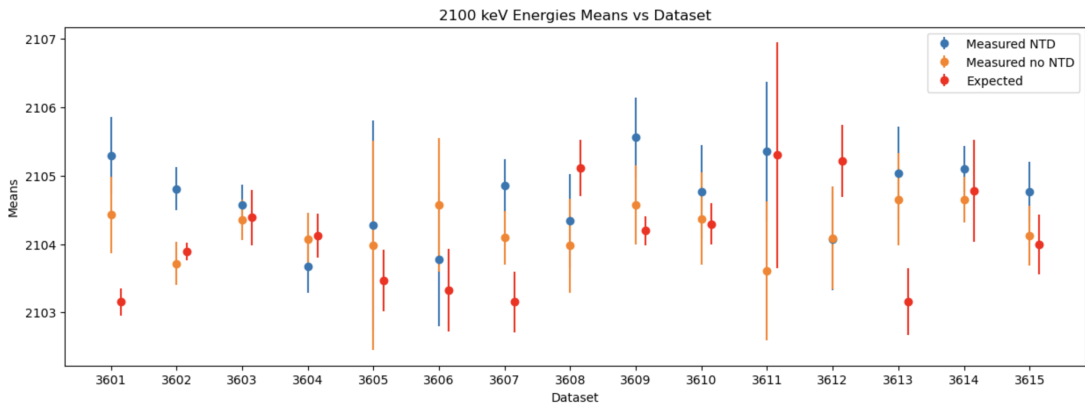


Figure 4.10: The 2100 keV CUORE detector calibration residuals compared to the fit parameters extracted for the Non-NTD Face and NTD Face events for each dataset.

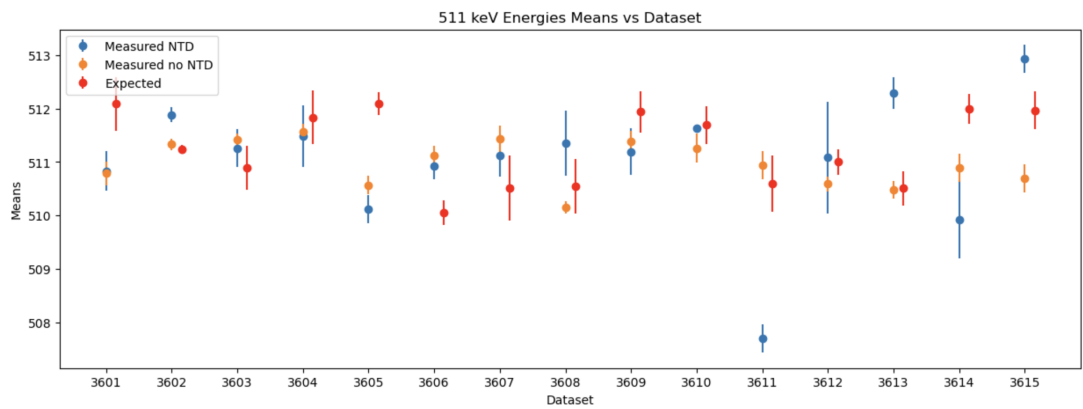


Figure 4.11: The 511 keV CUORE detector calibration residuals compared to the fit parameters extracted for the Non-NTD Face and NTD Face events for each dataset.

CHAPTER 5

CONCLUSION

In summary, the energy bias (difference between measured and expected energy) seems to depend on the event topology, and therefore, on the position of the event vertex within the crystal. This is most clearly seen for the 2104 keV line for both multiplicity 2 and 3 datasets which shows significant variation as a consequence of topology. Specifically, there seems to be larger energy reconstructed when the event vertex is close to the face containing the NTD, indicating more efficient phonon collection. This is the first definitive indication of the position dependence of reconstructed energy in TeO₂ thermal calorimeters.

5.1 Future Work

As stated previously, the discovery made here is an entirely new concept in the CUORE analysis framework that needs to be further understood. Proceeding forward this analysis would need to continued for double escape events, which have lower statistics. However, we have new data in the upcoming release of the 2-tonne-year dataset which would provide us with twice the statistics making re-analyzing the single energy escape events

and analysis of the double energy escape events more profound. Secondly, this work will be pushed towards constant collaboration with the CUORE detector performance working group on an algorithm for calibration corrections. Finally, we would also like to compare our findings with high-rate GEANT4 simulations to validate the conclusions made in this thesis.

BIBLIOGRAPHY

- [1] K. Alfonso et al. “Search for Neutrinoless Double-Beta Decay of ^{130}Te with CUORE-0”. In: *Physical Review Letters* 115.10 (Sept. 2015). ISSN: 1079-7114. DOI: 10.1103/physrevlett.115.102502. URL: <http://dx.doi.org/10.1103/PhysRevLett.115.102502>.
- [2] Frank T. Avignone, Steven R. Elliott, and Jonathan Engel. “Double beta decay, Majorana neutrinos, and neutrino mass”. In: *Rev. Mod. Phys.* 80 (2 Apr. 2008), pp. 481–516. DOI: 10.1103/RevModPhys.80.481. URL: <https://link.aps.org/doi/10.1103/RevModPhys.80.481>.
- [3] CUORE Collaboration. “An energy-dependent electro-thermal response model of CUORE cryogenic calorimeter”. In: *Journal of Instrumentation* 17.11 (Nov. 2022), P11023. DOI: 10.1088/1748-0221/17/11/P11023. URL: <https://dx.doi.org/10.1088/1748-0221/17/11/P11023>.
- [4] *CUORE: A search for neutrinoless double beta decay*. URL: <https://cuore.lngs.infn.it/en>.
- [5] Michelle J. Dolinski, Alan W.P. Poon, and Werner Rodejohann. “Neutrinoless Double-Beta Decay: Status and Prospects”. In: *Annual Review of Nuclear and Particle Science* 69.1 (Oct. 2019), pp. 219–251. ISSN: 1545-4134. DOI: 10.1146/

`annurev-nucl-101918-023407`. URL: <http://dx.doi.org/10.1146/annurev-nucl-101918-023407>.

- [6] Valentina Dompè. “Search for neutrinoless double beta decay of ^{128}Te with the CUORE experiment”. PhD thesis. Gran Sasso Science Institute, 2021.
- [7] Alexey Drobizhev. “Searching for the $0\nu\beta\beta$ Decay of ^{130}Te with the Ton-Scale CUORE Bolometer Array.” PhD thesis. University of California, Berkeley, 2018.
- [8] A. Giachero et al. *New results from the CUORE experiment*. 2021. arXiv: 2011.09295 [physics.ins-det].
- [9] Roger Guo Huang. “Searching for $0\nu\beta\beta$ Decay with CUORE and CUPID”. PhD thesis. University of California, Berkeley, 2021.
- [10] Jonathan Loren Ouellet. “The Search for $0\nu\beta\beta$ Decay in ^{130}Te with CUORE-0”. PhD thesis. University of California, Berkeley, 2015.
- [11] G Rajasekaran. *The Story of the Neutrino*. 2016. arXiv: 1606.08715 [physics.pop-ph].
- [12] *The Standard Model of particle physics*. URL: <https://physics.iitm.ac.in/faculty.php>.
- [13] Kai Zuber. “Status and perspectives of double beta decay searches”. In: *Journal of Physics: Conference Series* 578.1 (Jan. 2015), p. 012007. DOI: 10.1088/1742-6596/578/1/012007. URL: <https://dx.doi.org/10.1088/1742-6596/578/1/012007>.